The Rise and Fall of Satellites in Galaxy Clusters

Giuseppe Tormen

Max Planck Institute für Astrophysik, Karl-Schwarzschild-Strasse 1, 85740 Garching bei München - GERMANY and
Institute of Astronomy, University of Cambridge, Madingley Road, Cambridge CB3 0HA - UK
Email: bepi@mpa-garching.mpg.de

arXiv:astro-ph/9611078v2 23 Feb 1998

ABSTRACT
We use N-body simulations to study the infall of dark matter haloes onto rich clusters of galaxies. After identification of all cluster progenitors in the simulations, we select those haloes which accrete directly onto the main cluster progenitor. We construct the mass function of these merging *satellites*, and calculate the main orbital parameters for the accreted lumps. The average circularity of the orbits is $\epsilon \simeq 0.5$, while either radial or almost circular orbits are equally avoided. More massive satellites move along slightly more eccentric orbits, with lower specific angular momentum and a smaller pericentre. We find that the infall of satellites onto the main cluster progenitor has a very anisotropic distribution. This anisotropy is to a large extent responsible for the shape and orientation of the final cluster and of its velocity ellipsoid. At the end of the simulations, the major axis of the cluster is aligned both with that of its velocity ellipsoid, and with the major axis of the ellipsoid defined by the satellite infall pattern, to $\approx 30°$ on average. We also find that, in lower mass clusters, a higher fraction of the final virial mass is provided by small, dense satellites. These sink to the centre of the parent cluster and so enhance its central density. This mechanism is found to be partially responsible for the correlation between halo masses and characteristic overdensities, recently highlighted by Navarro, Frenk & White (1996).

Key words: cosmology: theory – dark matter

1 INTRODUCTION

In cosmological models of gravitational instability, structures form by the collapse of small perturbations of some initial density field. The most successful flavour of these models is the hierarchical clustering picture, where matter clusters on small scales first, and structures form in a bottom-up fashion. In this scenario, clusters of galaxies represent the most recently assembled structures, and are therefore dynamically young systems. For this reason, they are ideal candidates to study the link between the final structure and morphology of an object and its formation process. In this context, it is of great interest to investigate in some detail the accretion of matter within the proto-cluster. The study of the recursive merging of smaller size objects onto the main cluster progenitor is a powerful tool to unveil the cluster dynamical history, and can possibly help us to understand some details of its final structure.

A detailed investigation of the cluster merging history usually requires either Monte–Carlo techniques or numerical simulations. In the former case, one uses an analytical model for the clustering of structures, like the Press & Schechter (1974) (hereafter P&S) formalism, and extensions (Bond et al. 1991; Bower 1991; Lacey & Cole 1993; Lacey

& Cole 1994), to produce Monte Carlo realizations of the merging histories of dark matter haloes. These in turn are the starting point of a recipe for galaxy formation, whose predictions can be compared to the observed properties of real galaxies and clusters. Extensive work in this direction has been done in the past few years (Kauffmann & White 1993; Cole et al. 1994; Heyl et al. 1995; Kauffmann 1995), in an attempt to interpret the various observations in a unified and global framework. While this work provides a plausible link between the properties of dark matter haloes and those of galaxies and clusters, it is necessary to complement the investigation with numerical simulations. These, although limited to a smaller number of applications, do not need as many simplifying assumptions on the details of structure formation. Therefore one can address issues not accessible to Monte Carlo techniques, as the dynamical equilibrium of clusters, the study of their density and velocity profiles, the characterization of the orbits of infalling haloes, the survival times of haloes after merging with the main cluster, and others. These results are also useful to improve the Monte Carlo methods, as they can tell which assumptions are more realistic for the galaxy formation recipe.

Although many numerical simulations of cluster forma-

tion have been performed in the past (White 1976; Quinn, Salmon & Zurek 1986; Navarro, Frenk & White 1995; Tormen, Bouchet & White 1997) there is little work on the connection between the details of the cluster merging history and the final cluster configuration, in a cosmological context. One reason for this is that such analysis requires simulations with very high mass and force resolution, as only recently have become available. In the present paper we present the results of such a study. Using a sample of nine dark matter haloes of rich galaxy clusters, obtained from high resolution N-body simulations, we identify the merging history of all cluster progenitors, and extract from that a population of *satellites*, i.e. progenitor haloes accreting directly onto the most massive cluster progenitor at any time. We study this population and characterize its dynamical properties. We then use the information on the infalling satellites as a key to interpret the cluster formation history, and its final shape and structure. In a forthcoming paper (Tormen 1997, in preparation) we shall make a detailed comparison of the merging history of the clusters with the predictions of the extended P&S formalism.

The outline of the paper is as follows. Section 2 briefly presents the simulations, and describes the method used to define their halo population. In Section 3 we study the cluster satellites. We look at the way they merge with the main halo, and measure their mass distribution. Then, by moving the satellites in the spherically averaged, static potential of the main halo, as measured at each time output, we integrate their orbits and derive the main orbital parameters. In Section 4 we study the connection between shapes and orientations of clusters and the infall pattern of their satellites, and investigate the dynamical origin of universal dark matter density profiles (Navarro, Frenk & White 1996). Finally, in Section 5 we summarize the paper and present the main conclusions.

2   METHOD

2.1   Simulation setup

For the present analysis we use the N-body simulations presented in Tormen et al. (1997), where complete details on the simulations may be found. In summary, our sample consists of nine dark matter haloes of galaxy clusters, with an average mass of $1.13 \times 10^{15} M_\odot$, resolved by ≈ 20000 dark matter particles each within the virial radius, with an effective force resolution of ~ 25 kpc. The haloes come from an Einstein–de Sitter universe with scale-free power spectrum of fluctuations $P(k) \propto k^n$, and a spectral index $n = -1$, the appropriate value to mimic a standard cold dark matter spectrum on scales relevant to cluster formation. The simulations have a Hubble parameter $H_0 = 50$ km s^{-1} Mpc^{-1} and are normalized to match the observed local abundance of galaxy clusters (White et al. 1993). Each simulation was performed using two sets of particles, a first high resolution set to actually form the cluster, and a low resolution set of massive background particles to model the large-scale tidal field of the simulation out to a scale $L = 150$ Mpc. For each of the nine simulations we shall use ten outputs, ranging from $z \simeq 6$ to $z = 0$, for a total of 90 outputs.

2.2   Identification of dark matter lumps

The relatively low number of particles of each simulation ($N \approx 60000$ on average) allowed us to use the potential energy of particles to identify the location of dark matter lumps (Efstathiou et al. 1988). We defined lumps by an overdensity criterion, and included all particles within a sphere of mean overdensity $\delta_v = 178$, centred on the particle with lowest potential energy. The value δ_v corresponds to the virial overdensity in the model of a spherical top-hat collapse. We shall call virial radius r_v the corresponding radius of the lump. We identified all lumps with at least five particles within r_v.

In order to determine the minimum size of lumps to use in our analysis, we performed the following test. We selected, for each output of each simulation, all lumps formed by n particles, and looked at the fate of those particles in the next time output. The particles of a lump will now be part of other lumps. We took note of the largest fraction of lump relic that was found in a single halo, and looked at the distribution of such quantity. If all, or most, of a lump is found in another halo on the next time output, the lump is a dynamically consistent object. We performed the analysis for several values of n, from $n = 5$ up, and found convergence in the resulting main relic distribution for lumps with at least 8 particles. For such lumps, in 95 per cent of the cases the largest relic carried at least half of the original mass, and in 70 per cent of the cases it carried more than 80 per cent. On the other hand, almost 20 per cent of lumps with 5 particles were completely dissolved in the field by the next output. Therefore we chose to limit our analysis to lumps with at least eight particles within their virial radius. All remaining particles, including those in smaller lumps, will be generally referred to as *field particles*. Since we limit our analysis to lumps which are progenitors of the nine simulated clusters, these lumps are only made up with high resolution particles.

3   MERGING OF SATELLITES

Let us call, at any given redshift, *progenitors* of a cluster all haloes containing at least one particle that by $z = 0$ will be part of the cluster, and also all field particles which will end up in the final cluster. At any redshift, we define the *main* (or *largest*) *progenitor* of a cluster as the progenitor halo containing the largest number of particles which will be part of the final cluster. In all cases this coincided with the most massive progenitor halo, although, with the present definition, the main progenitor in a simulation is not necessarily the most massive one. To help clarifying the meaning of these terms, one can refer to the schematic merging history of halos given by the merging tree in Fig.6 of Lacey & Cole (1993).

We termed *satellites* those progenitor lumps which were directly accreted onto the main cluster progenitor. Operationally, we started from the list of progenitors at a given output of the simulation, and selected those haloes for which at least one particle was found in the largest cluster progenitor in the next time output of the simulation. We shall characterize these satellites by studying their mass distribution, and by calculating their orbital parameters. We shall call *identification time* t_{id} of a satellite the last output time
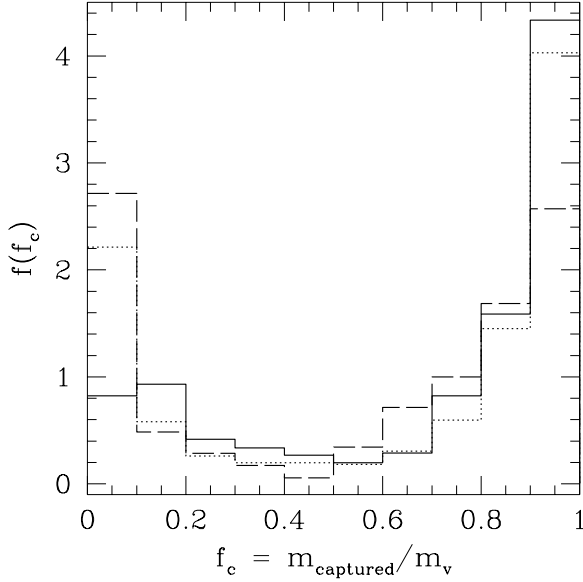
Figure 1. Number weighted distribution of the fraction of satellite mass which is captured by the main cluster progenitor. Each curve refers to a different range of particle number for the satellites: $m_v < 20$ particles (solid), $20 < m_v < 100$ particles (dotted) and $m_v > 100$ particles (dashed). The two extreme situations are most common: satellites stripped by a small amount of their mass, with $m_{captured}/m_v < 0.2$, and satellites captured (almost) entirely, with $m_{captured}/m_v > 0.8$. Intermediate cases are very rare.

before the satellite accretes onto the main cluster progenitor. Since we consider ten outputs for each simulation, there are nine outputs (all but the last) to identify satellites.

In the hierarchical clustering picture of structure formation, matter clusters on small scales first, and dark matter haloes of a given size are formed by the assembly of smaller haloes which were formed earlier. In this idealized model, when a satellite lump is accreted onto a more massive halo, all of the satellite mass is incorporated in the bigger object. Although this description is fairly close to what we observe in N-body simulations of hierarchical clustering, the actual collapse of structures is more complicated than its idealized version; in particular, satellites may be tidally stripped by the accreting halo, so that only a fraction of the satellite mass becomes part of the accreting system. This is clearly illustrated in Fig. 1, where we show the number distribution of the fraction f_c of satellite mass captured by the main cluster progenitor, for all time outputs and all clusters together. Each curve refers to satellites with different number of particles. We observe that most of the satellites transfer either very little or most of their mass to the main cluster progenitor, whereas less than 20 per cent of the satellites have $f_c \in [0.2, 0.8]$. This trend is more evident for more massive satellites. While this result may be partially due to a few satellites which, by chance, happen to cross the virial radius of the main progenitor at the time of a simulation output, it is more likely that the distribution reflects different physical situations. We shall address the issue at the end of the section on the orbital parameters.
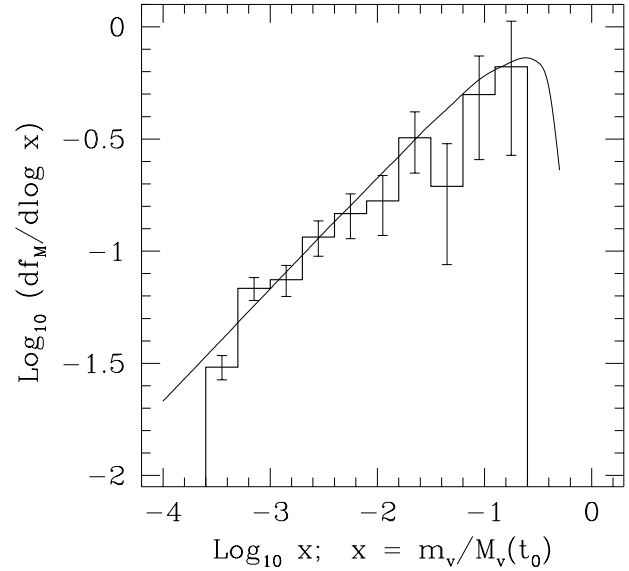

Figure 2. Mass function of satellites. The histogram shows the fraction of cluster mass accreted in satellites of mass $m_v/M_v(t_0)$, averaged over all clusters in our sample. Only haloes accreted after the cluster formation redshift z_f (the redshift when the most massive progenitor reaches half of the final cluster mass), and captured by at least 50 per cent of their virial mass, are considered. The mass of satellites is given in units of the *final* cluster mass; error bars are Poissonian. The solid curve is a prediction from Monte Carlo merging trees, taken from Lacey & Cole 1993 (their Fig. 12).

3.1 Mass function of satellites

It is interesting to look at the spectrum of masses that clumped together and formed the clusters in our sample. This will tell us, for example, how much of a cluster's mass was made up by violent encounters with massive satellites, as opposed to smooth accretion of small sized systems. We want to select from the satellite list those who significantly contribute with their mass to the formation of the cluster. We do this by eliminating all satellites captured by less than 50 per cent in mass, that is with $f_c < 0.5$. This choice seems reasonable, as Fig. 1 shows that there is a clear separation between satellites barely stripped and satellites really captured. Moreover, with this distinction, a satellite excluded from the selection in one output may be included in the next, if it is really captured by the main halo. We shall call *merging time* of the satellite onto the cluster the time when the satellite first crosses the virial radius of the main cluster progenitor. Since the separation between consecutive outputs of our simulations is $\Delta t \simeq 1.6$ Gyr, we can only bracket the estimated merging time of a satellite between the identification time t_{id} and the next output of the simulation at $t_{id} + \Delta t$.

Fig. 2 shows the mass distribution of satellites captured by at least 50 per cent in mass; the abscissa is the virial (i.e. total) mass of the satellite normalized to the final mass of the cluster. The smooth curve is taken from Lacey & Cole
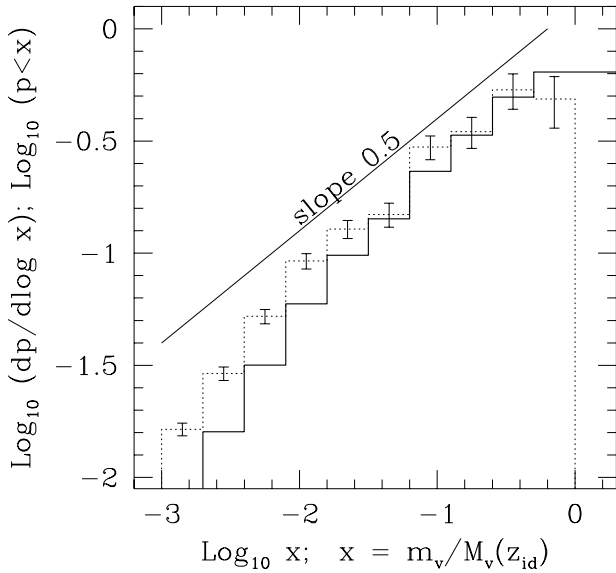
Figure 3. The same distribution shown in Fig. 2 is shown here with satellite masses normalized to the mass of the main cluster progenitor at the time of capture. Both the cumulative (solid line) and the differential (thin dotted line, with Poissonian error bars) are drawn. These curves show the relative occurrence of merging events with satellites of a given mass ratio $m_v(z)/M_v(z)$.

1993, and is the expected mass distribution of satellites obtained from Monte–Carlo merging histories of haloes. The prediction does not depend on the final cluster mass if one considers only the accretion events happening after the *formation redshift* z_f, defined as the redshift when the most massive cluster progenitor first reaches at least half of the final cluster mass (Lacey & Cole 1993, 1994). In our case, we only considered satellites with $z_{id} \leq z_f$. To give an idea of our statistics, there are roughly 1400 satellites merging with the clusters, of which almost 600 identified after z_f. The histogram is normalized to the fraction of cluster mass provided by the satellites with $f_c \geq 0.5$. This is done to keep account of the matter accreted onto the main cluster progenitor in both field particles and satellites with $f_c < 0.5$. The agreement between model and simulation data is very good, as the curve matches the histogram over nearly three orders of magnitude in mass.

In Fig. 2, the $x-$axis has masses normalized to the final mass of the clusters, for the purpose of comparing it with the Monte–Carlo prediction. However, it is more instructive to look at the same distribution normalizing masses to that of the main cluster progenitor at the identification time of the satellite, t_{id}. This is done in Fig. 3, where the differential (dotted histogram) and cumulative (solid histogram) mass functions of the accreted satellites are plotted. Now we use all satellites identified at any t_{id}, but always with $f_c \geq 0.5$. The (Poissonian) error bars refer to the differential distribution.

In the mass range $\log x \gtrsim -2$ the distribution follows a power law with slope 0.5, the same slope of the distribu-

tion in Fig. 2. Normalization is the same described above, showing that, on average, one third of the cluster mass was accreted either in field particles or in satellites captured by less than half of their mass. The next largest contribution, about 20 per cent of the final cluster mass, comes from encounters with satellites with mass ratio $m_v/M_v \geq 0.5$. On the whole, roughly $40--45$ per cent of the total cluster mass comes from encounters with satellites with $m_v/M_v \geq 0.1$. These figures are quite robust, as they remain essentially the same if we use in the histograms all satellites (regardless to the captured fraction of their mass) or if we use for the satellite mass the actual captured mass instead of the virial mass. How frequent are encounters with massive satellites? Let us consider only satellites with $f_c \geq 0.5$. The average number per cluster of encounters with satellites with mass ratio ≥ 0.1 ($\geq 0.2; \geq 0.5$ respectively) is 2.7 ± 0.5 (1.5 ± 0.4, 0.1 ± 0.1) from the time t_f when a cluster reached half of its final mass ($z_f \approx 0.5$ on average) to the present time, and 13.7 ± 1.4 (7.4 ± 1.0, 2.3 ± 0.5) over a Hubble time. Error bars are 1σ estimates from bootstrap resampling over the clusters. It has been shown (Tormen et al. 1997) that encounters with satellites with mass ratio larger than roughly 0.2 can perturb the *rms* velocity of the cluster by as much as 30 per cent within the virial radius. According to the present result, a rich cluster should undergo such encounters between one and two times since z_f.

3.2 Orbital parameters

In this section we study the orbits of the satellites which accrete directly on the main cluster progenitor. Since we want to investigate how satellites fall onto the cluster, we are interested in the *initial* orbital parameters, which define the orbits *prior* to the actual merging. Of course, after a satellite crosses the virial radius of the main cluster, different dynamical processes (tidal stripping, dynamical friction, encounters with other halos, etc...) become more relevant, and its orbit will be modified. However, the *initial* orbits are still very interesting as they trace the accretion process. Moreover, they can be used as an input for a more realistic modelling of the dynamical processes listed above, for example in semianalitic models of galaxy formation.

In order to integrate the orbits of satellites we used the static spherical potential approximation (e.g. Binney & Tremaine 1987, their Eq.(3.13)), and moved the satellites in the potential of the main cluster progenitor as measured at time t_{id}. The radial potential profile $\Phi(r)$ was obtained by averaging the actual potential of all the particles in each output in spherical shells of equal logarithmic width 0.05, centred on the main cluster progenitor. A further Gaussian filter, of logarithmic width 0.2, was applied to the profiles to make them smoother and so avoid multiple solutions in the orbital parameters. Although we calculated the orbital parameters for all satellites, here we shall only show results for satellites with $f_c \geq 0.5$.

The approximations made will lead sometimes to unrealistic solutions, especially *(a)* for massive satellites, whose contribution to the total potential is not negligible, and *(b)* at early times, when the main cluster progenitor grows faster, and so the static approximation is poorer, and when there is more chance of having big neighbouring haloes that invalidate the spherical approximation. In order to mini-

mize these problems, in this Section we limit our analysis to outputs where the main cluster progenitor has at least half of the cluster final mass, that is to redshifts $z_{id} < z_f$. With this choice, the mass of satellites, relative to that of the main cluster, is kept small (in our case $m_v/M_v < 0.25$ for more than 99 per cent of the satellites), and the static model is closer to reality, since the potential well of the cluster has already been built up. This selection will somehow bias our statistics, because we automatically exclude massive ($m_v/M_v \gtrsim 0.25$) satellites from the analysis. However, we prefer this choice to the alternative of including unreliable satellites in the results.

In order to compare results from different outputs and from different clusters, we need to rescale them to uniform units. In particular, lengths should be expressed in units of the virial radius of the main cluster progenitor. Now, even in a static potential, the virial radius R_v of the main halo will grow with time, since the mean background density of the universe is decreasing like $(1 + z)^3$. As a consequence, from the time t_{id} when we identify a satellite, and the later times t_v, t_p when the satellite crosses the virial radius and reaches the orbit pericentre, R_v will have grown, sometimes by a not negligible amount. This growth must be taken into account since our satellites are identified at different distances from the main progenitor, and so cross its virial radius at different times. For every satellite, we calculate t_v and $R_v(t_v)$ moving the satellite in the static potential of the cluster, and moving the cluster virial radius outward until the satellite crosses it.

A proof that the assumed model is a better approximation to the real clusters at late than at early times comes from the distribution of orbit pericentres: the most obvious unphysical result is a satellite not merging at all with the main cluster, that is, with a pericentre $r_p > R_v$. This actually happens for 14 per cent of the satellites with $z_{id} \geq z_f$, but only for 2 per cent of the satellites with $z_{id} < z_f$.

We must also be careful that the satellites are not too far from the main cluster progenitor at their identification time. In fact, at large distances from the cluster, orbits are more easily influenced by neighbouring massive objects, and the spherical average of the potential is no more a good description of the true field. Fortunately, in practice this is not a problem, since all selected satellites have $r_{id} < 3R_v(t_{id})$, and 90 per cent have $r_{id} < 2R_v(t_{id})$.

What is the shape of the orbits? How close do the satellites come to the centre of the main cluster? How much angular momentum do they carry? These are some questions we want to answer in this Section. Fig. 4 shows a scatter plot of the orbital circularity ϵ versus the pericentre of the satellite's orbit (the latter rescaled to the virial radius of the main cluster progenitor, $R_v(t_v)$, at the time of crossing it). The circularity $\epsilon \equiv J/J_c(E)$ (e.g. Lacey & Cole 1993) is the ratio of the angular momentum J of the orbit to that, $J_c(E)$, of a circular orbit with the same energy E. Radial orbits have $\epsilon = 0$, while $\epsilon = 1$ for circular ones. The figure shows that more eccentric orbits come closer to the cluster's centre, as naturally expected. The mean pericentric distance is $r_p/R_v(t_v) = 0.38 \pm 0.26$ ($1\,\sigma$ of the distribution). The distribution for ϵ has an average value of 0.53 ± 0.23. Almost radial or almost circular orbits are much less likely than intermediate ones. The mean amplitude of the 3-dimensional velocity of satellites as they cross R_v is $v_{sat}(R_v) = 1405 \pm 234$ km s^{-1}, with 5, 25, 50, 75 and 95 percentiles at 990, 1260,
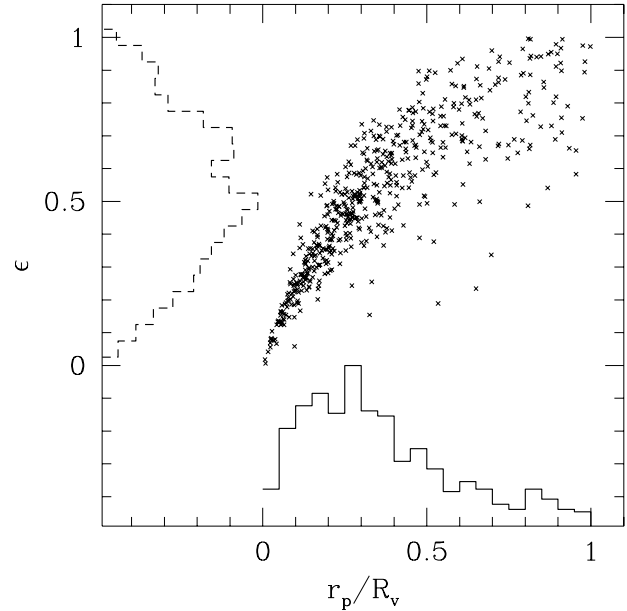

Figure 4. Scatter plot of the orbital pericentre r_p/R_v and the orbital circularity ϵ. The two histograms show the corresponding projected distributions (solid line for r_p/R_v and dashed line for ϵ).

1510, 1760 and 2200 km s^{-1} respectively. In terms of the circular velocity of the main halo at $R_v(t_v)$, the same velocity has 5, 25, 50, 75 and 95 percentiles at 0.77, 0.99, 1.12, 1.21 and 1.38 respectively.

We are now in the position to check if satellites only partially captured and satellites completely merged have different dynamical histories. One possibility is that the formers are on more circular orbits than the latters, so that only the satellite outskirts are tidally stripped by the main progenitor, and the rest of the satellite escapes. At the other extreme, satellites in more eccentric or radial orbits would be completely swallowed. For satellites in these two extreme situations we found average circularities $\epsilon(f_c < 0.2) = 0.55 \pm 0.01$ and $\epsilon(f_c > 0.8) = 0.527 \pm 0.007$ (1σ of the mean, now considering satellites at all t_{id}). Therefore the difference is not significant enough to explain the effect of Fig. 1. Another possible explanation is that satellites with $f_c \ll 1$ have already had a first encounter with the cluster, but they had enough kinetic energy to emerge from it once, leaving behind only part of their mass. The average 3-dimensional velocities when crossing R_v are, for the same subsets, $v_{sat}(R_v; f_c < 0.2) = 1370 \pm 23$ km s^{-1} and $v_{sat}(R_v; f_c > 0.8) = 1239 \pm 12$ km s^{-1} (1σ of the mean). Here the difference is more significant: indeed satellites captured by less than 20 per cent in mass have a higher speed, at a 3σ confidence level, than those completely captured. Perhaps a combination of this effect and of the former is responsible for the shape of the distribution shown in Fig. 1.

To see if there is any dependence of these and the other orbital parameters on the mass of the satellite (relative to the main cluster progenitor), we binned the data according to the relative mass of the satellite, m_v/M_v, where M_v
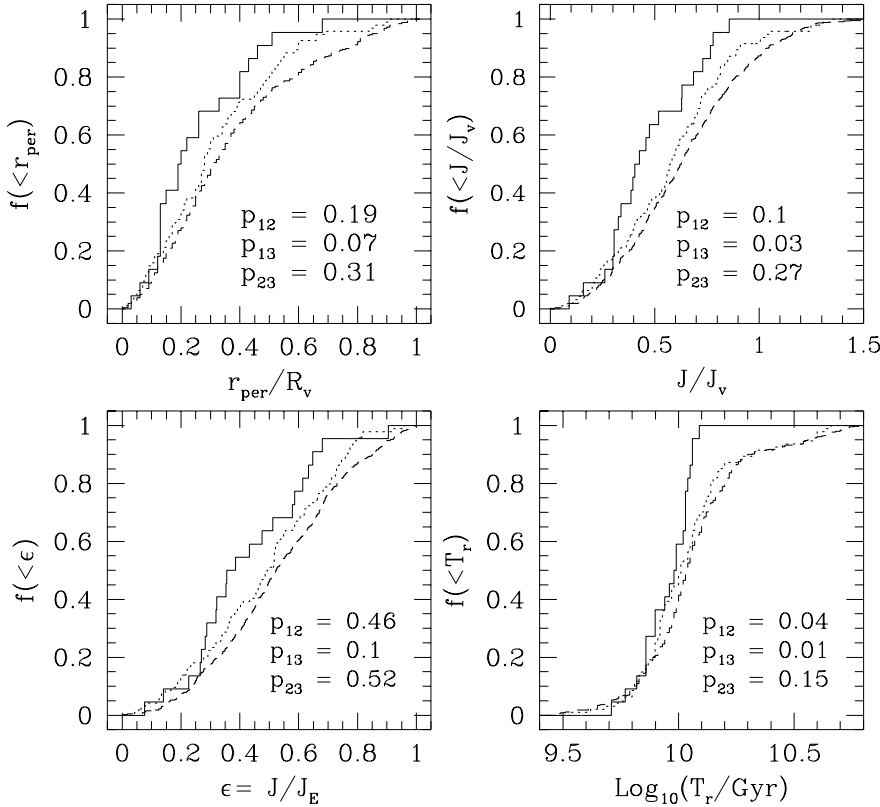
Figure 5. Dependence of some orbital parameter on the satellite mass. Each panel shows the cumulative distibution of a parameter, in three mass ranges: $m_v/M_v > 0.05$ (solid lines); $0.005 < m_v/M_v < 0.05$ (dotted lines) and $m_v/M_v < 0.005$ (dashed lines). Top Left: orbital pericentre r_p/R_v; Top Right: amplitude of the angular momentum, J/J_v; Bottom Left: orbit circularity ϵ; Bottom Right: radial period T_r/Gyr. In each panel, the numbers shown are the result of a KS test between every pair of distribution: p_{12} refers to the solid-dotted pair; p_{13} to the solid-dashed, and p_{23} to the dotted-dashed.

is calculated at the time t_v when the satellites cross R_v. The results are shown in Fig. 5, where we plot the cumulative distributions of r_p/R_v, of ϵ, of the amplitude of the angular momentum of the orbit relative to that of a circular orbit at the virial radius, J/J_v, and of the radial period T_r of the orbit. Data are binned in mass, in the three intervals $m_v/M_v < 0.005$, $0.005 < m_v/M_v < 0.05$, and $m_v/M_v > 0.05$. The figure shows some trend for more massive satellites to be on slightly more eccentric orbits, which penetrate deeper in the cluster, with lower (specific) angular momentum J/J_v and with a shorter orbital radial period T_r. We estimated the significance of these trends by a KS test performed on each pair of distributions. The probability of drawing such distributions by chance, from an identical underlying population, is given in each panel of the figure. This test shows that the trend with mass is statistically more significant for the radial period T_r and the amplitude of angular momentum J/J_v, and less for the pericentric distance r_p/R_v and the shape ϵ of the orbits. In the next Section we briefly discuss a possible explanation for these results, although we stress that these trends with mass are rather weak. An even weaker trend was also found for the kinetic energy of satellites as they cross R_v: more massive satellites approach the main halo at slightly lower speed than less massive ones. The effect is small, less than 10 per cent for the velocities, and is possibly due to dynamical friction. We finally looked

for dependence of these parameters on the mass of the final cluster, or on the time of identification t_{id}, but did not find any significant trend in the results.

4   DISCUSSION

4.1   Collapse anisotropy and shape analysis

Cosmological N-body simulations have shown that, in most scenarios, the gravitational collapse of matter happens first along pancakes, or sheet-like structures. Then filaments form, possibly at the intersection of different pancakes. Matter in these filaments collapses into dark matter haloes, and these flow along the filaments towards the potential minima, where they form galaxy clusters, perhaps at filaments' intersections. The collapse is therefore a highly anisotropic process. Recent observations of the distribution of substructure in X-ray clusters (West, Jones & Forman 1995) seem to indicate that anisotropic collapse is common also in real clusters. West et al. (1995) suggest that this anisotropic formation may be responsible for the shape and orientation of clusters with the surrounding large-scale structure, on scales $\sim 10h^{-1}$ Mpc, which is observed in different samples (e.g. Binngeli 1982; West 1989; Plionis 1994). A similar alignment is also found in cosmological N-body simulations (West, Villumsen & Dekel, 1991; Splinter et al, 1997). The link between

cluster shapes and merging histories has been addressed in the past (van Haarlem & van de Weygaert 1993). It is also recognized that some alignment exists between the cluster body and its velocity ellipsoid (e.g. Warren et al. 1992).

The high resolution of our simulations, together with the knowledge of their complete merging history, allows us to address the issue in a more direct and quantitative way than in previous work. We proceed as follows. For each cluster of our sample, we first found the principal axes of the cluster mass distribution, and of its velocity ellipsoid, by diagonalizing the mass tensor I_{ij} and the velocity dispersion tensor σ_{ij}^2:

$$I_{ij} = \sum_k (x_{k,i} - \bar{x}_i)(x_{k,j} - \bar{x}_j), \tag{1}$$

$$\sigma_{ij}^2 = \sum_k (v_{k,i} - \bar{v}_i)(v_{k,j} - \bar{v}_j), \tag{2}$$

where k labels particles and i, j are the Cartesian components of the vectors. Since all particles are identical, their mass does not appear in the expression of I_{ij}. The vector $\vec{x}$ identifies the cluster centre, and the mean velocity $\vec{v}$ is calculated using all the particles inside $0.5R_v$ to limit the bias from infalling substructure. The sums are extended to all particles within the virial radius. Although this choice has been shown to systematically underestimate the true axial ratios (Warren et al. 1992), this is not relevant for the main purpose of the present analysis.

To characterize the infall pattern we similarly defined the mass tensor of the satellite distribution:

$$\hat{I}_{ij} = \sum_k \hat{x}_{k,i} \hat{x}_{k,j} m_{k,v}. \tag{3}$$

Here $\hat{x}$ is the unit vector pointing in the direction (θ, ϕ) of approach of the satellite towards the main cluster progenitor. This direction is measured at time t_{id}, just before the merging of the two. Each contribution to $\hat{I}_{ij}$ is now weighed by the satellite's virial mass m_v. The reference system is centred on the main cluster progenitor.

We then compared the shapes of the three ellipsoids and the relative orientations of the three major principal axes. Shapes can be classified using the triaxiality parameter (Franx, Illingworth & de Zeeuw 1991):

$$T = \frac{(a^2 - b^2)}{(a^2 - c^2)}, \tag{4}$$

where $a \geq b \geq c$ are the three principal axes of the ellipsoid. We shall call *oblate* ellipsoids with $0 < T < 1/3$, *triaxial* those with $1/3 < T < 2/3$, and *prolate* those with $2/3 < T < 1$ (Warren et al. 1992), and will label T_C, T_V and T_S the triaxiality parameters referring respectively to the cluster shape, to its velocity dispersion ellipsoid and to its satellite distribution as defined above. We quantify the alignment in the orientation of two ellipsoids E_1 and E_2 using the cosine of the (3 dimensional) misalignment angle between the two major axes a_1 and a_2, defined by $\cos(\Delta) = \cos\theta_1 \cos\theta_2 + \sin\theta_1 \sin\theta_2 \cos(\phi_2 - \phi_1)$. This is uniformly distributed in $[0, 1]$ for a random distribution of angles. Values larger than 0.5 (corresponding to misalignment angles smaller than $60°$) indicate a correlation in orientation.

In order to study the time evolution of shapes and orientations, we calculated them at two different times: at redshift
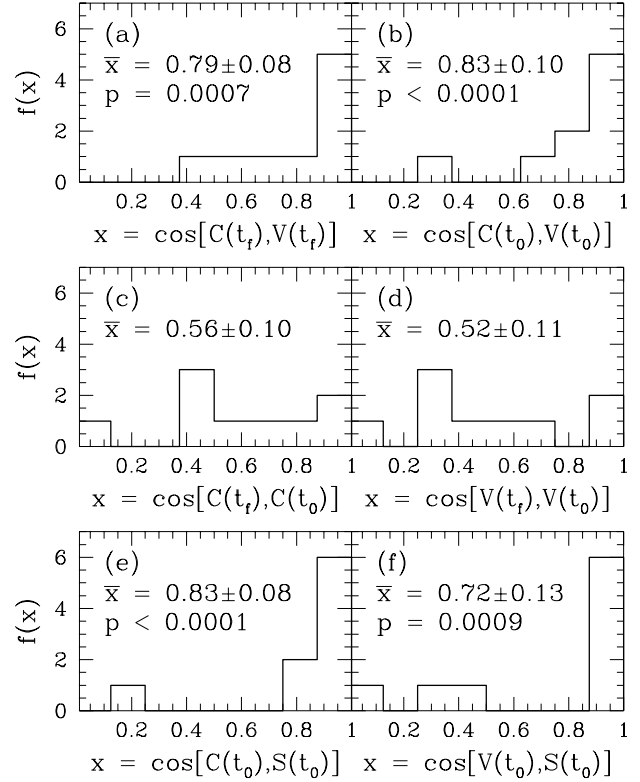

Figure 7. Orientation correlations between the major axes of the cluster shape (C), its velocity ellipsoid (V) and the distribution of its satellites (S). Each panel shows the distribution of the cosine of the misalignment angle for a pair of axes, and is labelled with the mean and 1σ of the mean. In the relevant cases we also give the probability p of obtaining the measured mean alignment from randomly oriented vectors.

$z = 0$ and at redshift z_f when the main cluster progenitor first assembled half of the final cluster mass. We only consider satellites identified at $z \leq z_f$. We do so because for $z > z_f$ the most massive progenitor may be on different branches of the merging tree at different redshifts. In such a case one cannot relate the satellite infall to the halo shape. Moreover, at early times satellites are identified at larger distances from the main halo, in units of its virial radius, and the direction of infall is less well determined due to possible perturbations on the orbits.

The results of our analysis are presented in Figs 6 and 7, and in Table 1. They refer to satellites with $f_c \geq 0.2$. Fig. 6 correlates, for each cluster of our sample, the triaxiality parameter of the cluster shape, that of its velocity dispersion and those of the satellite distribution. Fig. 7 does the same for the cosine of the misalignment angle $\cos(\Delta)$. Table 1 gives the ratio of major to minor axis for each considered ellipsoid.

From the figures and the table we can make the following comments. The cluster shape and velocity ellipsoids are preferentially prolate or triaxial, and somewhat correlated in shape, at early times (Fig. 6a). As evolution proceeds, shapes do not significantly evolve. Although the correlation improves from Fig. 6a to Fig. 6b, this change is not statistically significant according to a standard KS test. Table 1 shows that the elongation of cluster shapes and of their ve-
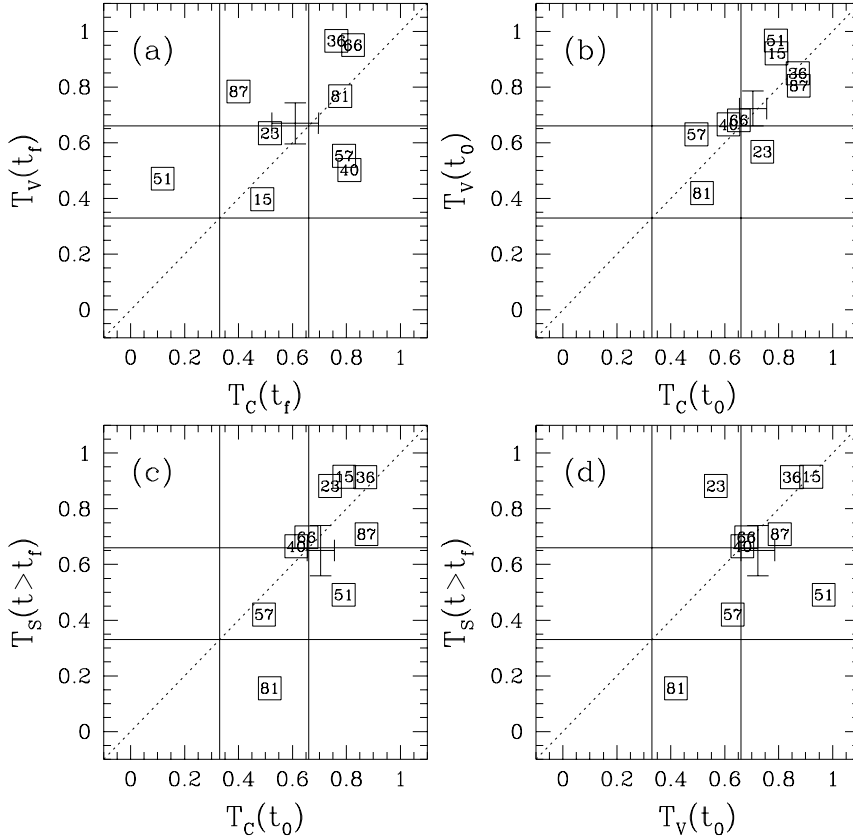
Figure 6. Shape Correlations between the cluster (C), its velocity ellipsoid (V) and the distribution of its satellites (S). Each number labels a cluster. Panel (a) compares the shape of the cluster and that of its velocity ellipsoid at redshift z_f when the main cluster progenitor first assembled half of the final cluster mass. For our simulations $z_f \approx 0.5$. Panel (b) does the same at $z = 0$. Panels (c) and (d) correlates the spatial and velocity structure of the cluster at $z = 0$ with the distribution of infalling satellites for $z < z_f$. The grid in each panel separates region corresponding to different shapes: oblate ($T < 1/3$), triaxial ($1/3 < T < 2/3$) and prolate ($T > 2/3$). The error bars indicate the mean $\pm 1\sigma$ of the mean for each distribution.

Table 1. Ratio a/c of longest to shortest axis for the cluster shape ellipsoid (C), for its velocity ellipsoid (V) and for the ellipsoid defined by the infall pattern of satellites (S). For each ratio, the mean $\pm 1\sigma$ of the mean is given.

Label	a/c t_f	a/c t_0
C	1.57 ± 0.08	1.60 ± 0.06
V	1.45 ± 0.06	1.32 ± 0.05
S	-	3.16 ± 0.30

locity ellipsoids do not appreciably change in time. A strong shape–velocity correlation is shown in the axes orientation, both at early and late times (Fig. 7a,b). By the present time the mean misalignment between the cluster shape and its velocity ellipsoid is of the order of $30°$, with a very high statistical significance.

On the other hand, both the cluster and its velocity ellipsoid change orientation in time, so that there is no very

significant correlation between the cluster orientation at t_f and that at t_0 (Fig. 7c), and between the corresponding velocity ellipsoids (Fig. 7d).

The final cluster shape is strongly aligned ($\approx 30°$ on average) with the infall pattern of satellites accreted after t_f (Fig. 7e). The shapes also are similar (Fig. 6c). A similar correlation is observed for the relative alignment of the velocity ellipsoid and of the satellite pattern (Fig. 7f). The shapes are correlated in that they tend to avoid oblate configurations (Fig. 6d). The satellite pattern is prolate or triaxial in eight clusters out of nine. The axial ratio a/c in Table 1 indicates a very anisotropic infall.

The same analysis on the orientation of the minor and intermediate axes of the ellipsoids gives a picture consistent with these results. In particular, it appears that the major and intermediate axes of an ellipsoid may sometimes switch during cluster evolution, causing anticorrelations similar to those observed in Fig. 7c,d. The minor axis instead remains rather well defined.

To summarize, the present results show that the

anisotropic infall of matter on the forming cluster is to a large extent responsible both for the final cluster shape and for its velocity structure. Both are strongly correlated, in shape and orientation, with each other and with the infall pattern of merging satellites. In their analysis, van Haarlem & van de Weygaert (1993) found that the cluster orientation is mainly determined by the last infalling subcluster. Although our results are in general agreement with theirs in highlighting the origin of such orientation, the present analysis suggests that cluster alignments are stable enough to be observed for a long time, as the correlations we found reflect the whole cluster history after its formation at $z_f \approx 0.5$.

Even if we have not directly checked the alignment of our clusters with the neighbouring large-scale structure, our analysis strongly suggest this picture, since the infalling satellites are tracers of the matter distribution around the clusters. Therefore our results are fully consistent with the alignments observed between clusters and the surrounding structure on scales $\sim 10h^{-1}$ Mpc, and favour an explanation of these in terms of structure accretion along preferred directions, e.g. along filaments. The shape and orientation of clusters would then be mainly determined by the large-scale initial density field.

This conclusion may also explain the trend in the orbital parameters shown in Fig. 5. Massive satellites are more likely to reside in dense filaments than less massive ones. Therefore, the formers should approach the main cluster progenitor along more eccentric orbits than the latters, with lower specific angular momentum and a closer pericentric distance, as indeed found.

4.2 Universal density profiles

Navarro et al. (1996) have recently found that dark haloes from their cold dark matter simulations exhibit remarkable similarity in shape, over a wide range of masses. After rescaling lengths in units of the halo virial radius R_v, they could fit the dark matter density profile of objects from the size of dwarf spheroidals to that of galaxy clusters using the one parameter fit

$$\frac{\rho(r)}{\rho_b} = \frac{\delta_s}{(r/r_s)(1 + r/r_s)^2}. \tag{5}$$

The free parameter is the *scale radius* r_s, which in turn determines the characteristic halo overdensity δ_s, defined by Equation (5). Navarro et al. (1996) found that, expressing halo masses in terms of the characteristic non-linear mass M_* corresponding to a linear overdensity of order unity, more massive haloes have larger scale radii, i.e. larger values of r_s/R_v, or equivalently have lower characteristic overdensity δ_s. Further work (Cole & Lacey 1996; Tormen et al. 1997, Navarro, Frenk & White 1996b) have confirmed this trend and extended the result to different cosmological models. This behaviour is in fact consistent with the expectations of hierarchical clustering, where structures form in a bottom-up fashion. Since at earlier times the universe was denser, one expects that less massive haloes, which formed earlier, have higher characteristic density δ_s, while more massive haloes, which form later from the merging of less massive ones, have lower values of δ_s. Navarro et al. (1997) link the characteristic density of a halo to the epoch when its progenitors first collapsed. They find a good agreement between their numerical results and the analytical predictions of the extended P&S formalism. Note however that Navarro et al. define the formation redshift of a halo in a way different from ours.

A physical mechanism for the shape of a universal dark matter profile has been recently proposed by Syer & White (1996). In their model, the density profile of a cluster is determined by the properties of its merging satellites. In particular, satellites dense enough to survive the tidal stripping of the parent cluster remain self-bound while they sink to the cluster centre, dragged by dynamical friction, and are therefore responsible for the inner shape of the halo density profile. This idea, together with the hierarchical clustering model, potentially provides a deeper explanation for the empirical relation between mass and characteristic density of haloes. Since we have reconstructed the merging history of all our simulated clusters, it is easy to test the idea directly.

We first need a definition to identify the matter in the dense cores of satellites. For this we take an overdensity threshold δ_t, which will always be referred to the mean background density at $z = 0$. This is important, since we need to compare the density of satellites identified at different redshifts with the density of the final cluster, and we must put all haloes on equal footing. For the present analysis we took $\delta_t = 10^5$. Each satellite, identified at any redshift, has some fraction of its mass above δ_t. This we shall call the mass in *satellite cores*. We shall say that a satellite is *denser* than another if a larger fraction of its total mass is stored in its core, as just defined. By analogy, the mass above the threshold δ_t in the final clusters: M_{δ_t}, will be referred to as mass in *cluster cores*.

We show in Fig. 8 some correlations between different quantities derived both from the final clusters and from their population of satellites. We used satellites identified at any time, and with $f_c > 0.2$. Looking at the figure, we can make the following statements.

(i) Less massive clusters are more centrally concentrated (Fig. 8a): the fraction M_{δ_t}/M_v of cluster mass above the fixed overdensity $\delta_t = 10^5$ at $z = 0$, that is the fraction of mass confined in the *cluster core*, is inversely proportional to the total cluster mass M_v.

(ii) Less massive clusters usually form at higher redshift (Fig. 8b): however, the scatter in the relation is fairly big. The correlation does not improve if one tries other definitions of formation time, e.g. changing the fraction of mass required in the most massive progenitor from the usual value of 50 per cent.

(iii) The fraction $M_{\delta_t}(sat)/M_v$ of cluster mass provided by satellite cores is proportional to the final fraction M_{δ_t}/M_v of mass in the cluster core (Fig. 8c). Therefore, the same fraction $M_{\delta_t}(sat)/M_v$ is inversely proportional to the final cluster mass (Fig. 8d).

(iv) The last correlation implies the correlations between $M_{\delta_t}(sat)/M_v$ and the scale radius of the profile, r_s/R_v (Fig. 8e). The original correlation between scale radius and final cluster mass (as in Tormen et al. 1997, their Fig. 16) is reproduced in Fig. 8f.

Notice that, while the correlation involving the scale radius implies a fit to the profile, the others, and in particular that of Fig. 8a, is model independent as is directly measured from the mass profiles.
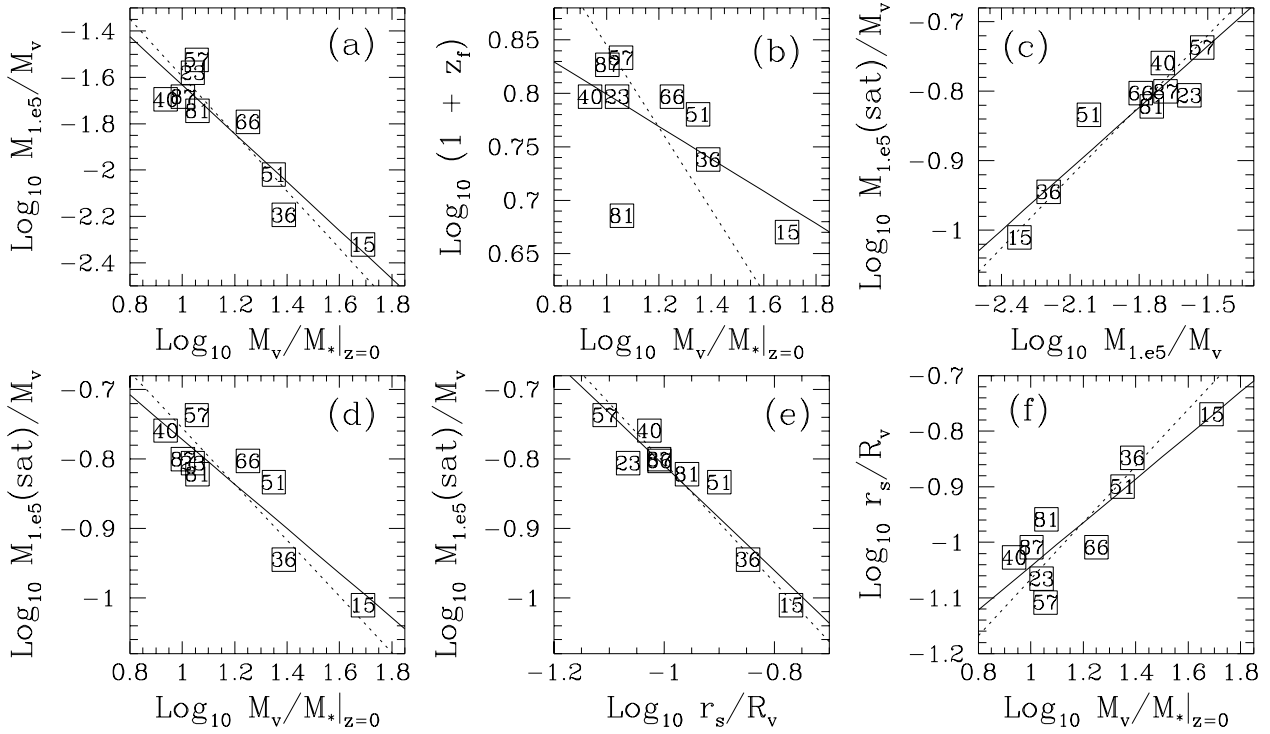
Figure 8. Correlations between the cluster virial masses M_v, the fraction of cluster mass in cluster cores $M_{1.e5}/M_v$, the fraction of cluster mass which was in satellite cores $M_{1.e5}(sat)/M_v$, the cluster formation redshift z_f and the scale parameter r_s of the cluster density profile. $M_* = (4/3)\pi R_*^3 \rho_b$ is the characteristic non-linear mass of the model, with ρ_b the mean background density of the universe and R_* the scale corresponding to a linear matter overdensity $\delta(R_*) = 1.69$. Each number labels a cluster. The two straight lines are equal weighted-least square fits of the direct (solid) and inverse (dotted) relation. The difference in their slope gives an idea of the goodness of the correlation. Definitions of the plotted quantities and details on the figure are given in the text.

Let us now focus on the correlation of Fig. 8d, and try to identify which factors determine it. Is it the mass of satellites? Their density? Their merging redshift? Their number? Or what combination of these? To answer this, we need to look in more detail at the characteristics of the satellite population. These are shown in Fig. 9. We first note, from Fig. 9a, that smaller satellites are usually denser, that is a higher fraction of their total mass comes from their *cores*, as defined above. This trend is also seen at any fixed time. Secondly, Fig. 9b shows that, on average, smaller clusters form from smaller (in physical units) satellites. The error bars are $\pm 1\sigma$ of the mean values. From these two results we may expect that smaller clusters form from denser satellites. This is indeed shown in Fig. 9c. Now, satellites in smaller cluster are smaller in absolute terms, but they are actually more massive if rescaled to the virial mass of the clusters. Therefore, since they are also denser, on average each of them brings to the final cluster mass M_v a larger contribution of mass from *satellite cores*. This is clearly shown in Fig. 9d. The next panel, Fig. 9e, shows that smaller clusters accrete, on average, a smaller number of satellites. We recall that this is not an effect of numerical resolution, as each cluster in our sample is resolved by roughly the same number of particles, and we consider in all cases satellites with at least 8 particles. The average contribution from each

satellite, given in Fig. 9d, times the total number of satellites, given in Fig. 9e, give exactly the total contribution in mass from satellite cores, given in Fig. 8d. This shows that the higher density of satellites merging onto smaller clusters wins over their slightly lower number.

We finally ask: how relevant to this result is the formation redshift of the cluster? If an object forms earlier, it will accrete on average smaller, and denser, satellites. One way to answer the question is to look at Fig. 8b: on average, the largest progenitor of smaller clusters is assembled earlier. However, the distribution of formation redshift predicted by the extended P&S formalism is fairly wide, and we noted that the correlation in Fig. 8b is not very tight. So we see clusters of very different mass which form almost at the same time, like clusters labelled 81 and 15, or 40 and 51. However, the same pairs of clusters have very different values for M_{δ_t}/M_v, and fairly different values of $M_{\delta_t}(sat)/M_v$, as well as different scale radii for their density profiles (Fig. 8f). A different way to address the same question is to measure the average redshift at which the cluster final mass was accreted. This is just the average value of the mass-weighted identification redshift of the satellite population: $< z_{id} m_v >$, with m_v the satellite virial mass. We can also measure the corresponding average redshift weighted by the mass in satellite cores: $< z_{id} m_{\delta_t} >$. Both values are shown in Fig. 9f, ver-
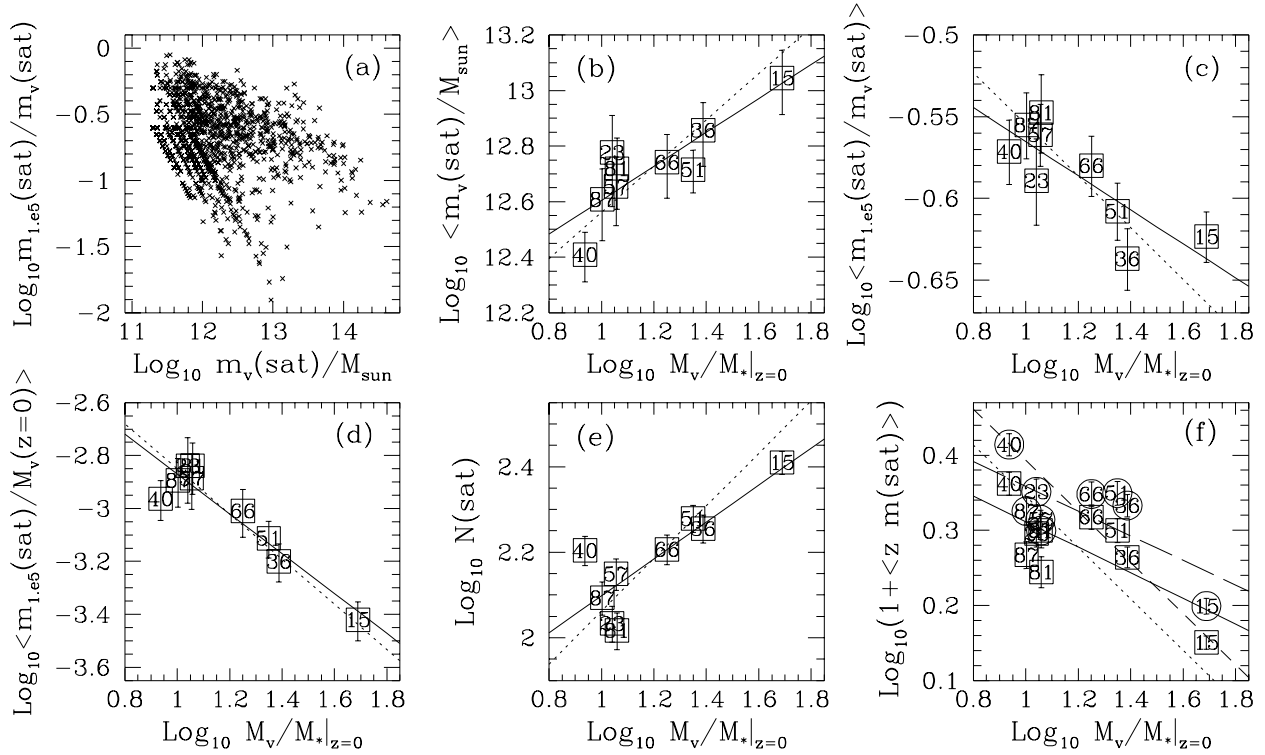
Figure 9. Correlations between satellite properties and mass of the final cluster. The straight lines are equal weighted-least square fits of the direct (solid) and inverse (dashed) relation. The difference in their slope gives an idea of the goodness of the correlation. Each number label refers to a cluster. Error bars are $\pm 1\sigma$ of the mean. In panel *(f)*, squares are mass weighted by m_v, the virial mass of satellites. Circles are mass weighted by m_{δ_t}, the satellite mass above an overdensity threshold $\delta_t = 10^5$. In this panel, the solid and dotted lines refer to the squares, while long dashed and short dashed lines fit the circles.

sus the final cluster mass M_v. The figure shows roughly the same trend of Fig. 8b, as expected, but here the scatter in the relation is even larger than there. Therefore the redshift of formation, or the average redshift of the mergers, is less important than the intrinsic density of satellites in producing the result of Fig. 8d.

To summarize, we have seen that, compared to more massive clusters, in less massive ones a higher fraction of the final mass comes from satellite cores, i.e. is provided by denser satellites. These satellites are denser because they are smaller, and not necessarily because they are accreted earlier. Moreover, their cumulative result is due to their density, not to their number. We repeated the analysis above using different values for the density treshold δ_t, and found that, in order to reproduce the result, δ_t must be larger than the typical density at the scale radius, but small enough to be accessible by the resolution of the simulation.

To further show that the mass from satellite cores is directly responsible for enhancing the central cluster density, we compare in Fig. 10 the density profile of all particles at $z = 0$ (solid curve) to the density profiles, always at $z = 0$, calculated using only the particles from satellite cores. All profiles are averaged over the cluster sample. The dotted curve refers to satellites merged before the formation redshift z_f, the short-dashed to satellites merged after z_f, and the long-dashed to all satellites, regardless to their merging

time. The figure shows that matter coming from satellite cores is more centrally distributed than the average matter in the clusters. Among the former, particles merged at earlier times have been heated by later mergings, and are less centrally concentrated. Instead, particles merged more recently have a higher central density, but also a larger spreading at large radii, possibly because they are less in equilibrium with the cluster potential. Quantitatively, the ratio between the half-mass radius of the mass from satellite cores and that of the whole cluster is $r_{hm}(sat)/r_{hm}(clu) = 0.45$, 1.12, 0.72 for satellites merged at $z > z_f$, $z \le z_f$ and at any z respectively. No difference is found in the velocity structure of the different particle sets. Therefore, particles coming from the cores of satellites are more bound to the final system than other particles. This confirms the interpretation of the secondary infall picture as a conservation of the binding energy ranking (Quinn & Zurek 1988; Zaroubi et al. 1996).

Finally, the ratio $M_{\delta_t}(sat)/M_v$ is only part of the story, and other parameters are likely to be important in determining the final structure of the cluster profile. For example, clusters labelled 23 and 51, which accrete a similar fraction of mass in satellite cores, have very different characteristic density and scale radius (Fig. 8a,d and f). However, the present result makes an important link between the cluster dynamical history and its final structure, as it shows that the sinking of dense satellites in the centre of their parent
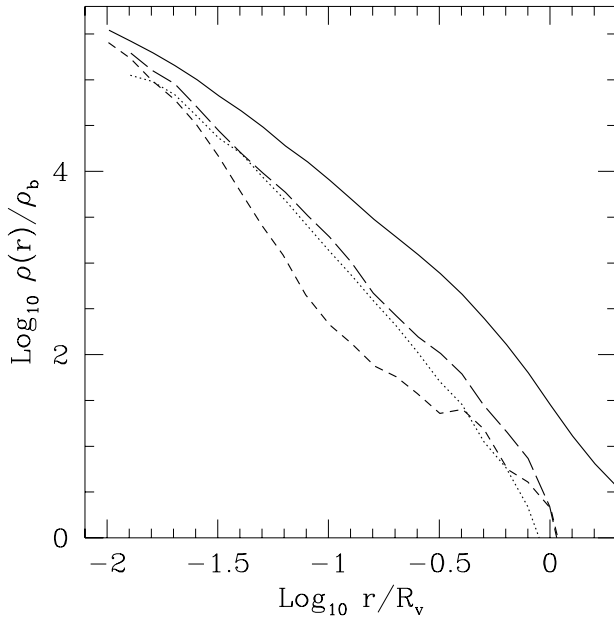
Figure 10. Dark matter density profiles at $z = 0$. The solid curve is the profile obtained by using all the particles in the cluster halo. The other curves were obtained by using only the particles that were in satellite cores. The dotted line is for satellites merged at $z > z_f$, the short dashed line for $z < z_f$, the long-dashed line for all satellites. All profiles are an average over the whole cluster sample. Particles from satellite cores are clearly more bound than the average particles. Further discussion is given in the text.

system is a relevant mechanism to giving the cluster its final density profile. As far as this mechanism is concerned, less massive clusters are more centrally concentrated because a larger part of their mass comes from denser satellites.

5   SUMMARY AND CONCLUSIONS

We have analysed the merging of satellites in N-body simulations of a sample of rich galaxy clusters. After identification of all cluster progenitors, we selected those haloes infalling directly onto the main cluster progenitor. We investigated the mass distribution of these *satellites*, and derived the main parameters for their orbits. Finally, we applied these results to two problems relevant to cluster formation. The first is the relation between the cluster final shape, its velocity ellipsoid, and the spatial pattern of the infalling satellites, a link that can explain the observed alignment of galaxy clusters with the surrounding large-scale structure. The second is the correlation between mass and characteristic overdensity of dark matter haloes.

The main conclusions of this paper may be summarized as follows.

(i) The mass function of satellites, i.e. of dark matter haloes merging directly onto the main cluster progenitor, is in very good agreement with the predictions based on Monte Carlo merging trees (Lacey & Cole 1993). Satellites fall onto the main progenitor along orbits with average cir-

cularity $\epsilon \simeq 0.5$, avoiding radial orbits as much as almost circular ones, and have a mean pericentre at $r_v \simeq 0.38 R_v$. More massive haloes tend to fall along more eccentric orbits, carrying a smaller specific angular momentum and reaching farther into the cluster.

(ii) The infall of satellites has a very anisotropic distribution. Its pattern is to a large extent responsible for the final shape and orientation of the cluster and of its velocity ellipsoid. At redshift $z = 0$ the major axis of the cluster mass distribution is aligned to the major axis of the cluster velocity ellipsoid to $\approx 30°$ on average. The cluster is also aligned with the ellipsoid defined by the satellite infall to $\approx 30°$ on average. A similar alignment exists between the satellite infall and the final velocity ellipsoid of the cluster.

Since this infall reflects the whole cluster history after the formation redshift at $z_f \simeq 0.5$, the pattern is stable enough to provide an explanation for the observed alignment between galaxy clusters and the surrounding large-scale structure, as recently suggested by the observations of West et al. (1995). This result confirms and quantifies the picture, often seen in N-body simulations, of galaxy clusters forming from haloes which flow preferentially along filaments. Clusters shapes and orientations would then reflect the large-scale initial density field. The same picture provides a possible natural explanation of why massive satellite are accreted along more eccentric orbits than less massive ones, as we found in our orbital analysis. This is because they are more likely to reside along dense filaments than less massive satellites. Therefore, the filamentary structure acts as a sort of focussing rail which drives massive satellites towards the cluster.

(iii) The properties of the population of satellites infalling onto the cluster influence also the final shape of its dark matter density profile. Lower mass clusters have a larger fraction of their total mass supplied by smaller and denser satellites. This mechanism is to some extent responsible for the correlation between the cluster final mass and the characteristic overdensity of its profile, observed by Navarro et al. (1996).

REFERENCES

Binney J., Tremaine S., 1987, Galactic Dynamics. Princeton University Press.
Binggeli B., 1982, A&A, 107, 338
Bond J.R., Cole S., Efstathiou G., Kaiser N., 1991, ApJ, 379, 440
Bower R.G., 1991 MNRAS 248, 332
Cole S., Lacey C.G., 1996, MNRAS, 281, 716

Cole S., Aragòn Salamanca A., Frenk C.S., Navarro J.F., Zepf S.E., 1994, MNRAS, 271, 781

Efstathiou G., Frenk C.S., White S.D.M., Davis M., 1988, MN-RAS, 235, 715

Franx M., Illingworth G., de Zeeuw T., 1991, ApJ, 383, 112

Heyl J.S., Cole S., Frenk C.S., Navarro J.F., 1995, MNRAS, 274, 755

Kauffmann G., 1995, MNRAS, 274, 160

Kauffmann G., White S.D.M., 1993, MNRAS, 261, 921

Lacey C.G., Cole S., 1993, MNRAS, 262, 627

Lacey C.G., Cole S., 1994, MNRAS, 271, 676

Navarro J.F., Frenk C.S., White S.D.M., 1995, MNRAS, 275, 720

Navarro J.F., Frenk C.S., White S.D.M., 1996, ApJ, 462, 563 (NFW)

Navarro J.F., Frenk C.S., White S.D.M., 1996b, astro-ph/9611107

Plionis M., 1994, ApJS, 95, 401

Press W.H., Schechter P., 1974, ApJ, 187, 425

Quinn P.J., Zurek W.H., 1988, ApJ, 331, 1

Quinn P.J., Salmon J.K., Zurek W.H., 1986, Nat, 322, 329

Splinter R.J, Melott A.L., Linn A.M., Buck C., Tinker J., 1997, ApJ, 479, 632

Syer D., White S.D.M., 1996, submitted to MNRAS

Tormen G., 1998, MNRAS, in press

Tormen G., Bouchet F.R., White S.D.M., 1997, MNRAS, 286, 865

van Haarlem M., van de Weygaert R., 1993, ApJ, 418, 544

Warren M.S., Quinn P.J., Salmon J.K., Zurek W.H., 1992, ApJ, 399, 405

West M.J., 1989, ApJ, 347, 610

West M.J., Jones C., Forman W., 1995, ApJ, 451, L5

West M.J., Villumsen J.V., Dekel A., 1991, ApJ, 369, 287

White S.D.M., 1976, MNRAS, 177, 717

White S.D.M., 1996, in Lahav O., Terlevich R., eds., Gravitational Dynamics. Cambridge University Press

White S.D.M., Navarro J. F., Evrard A.E., Frenk C.S., 1993, Nat, 366, 429

Zaroubi S., Naim A., Hoffman Y., 1996, ApJ, 457, 507